Supporting Information for "Room temperature magnetically ordered polar corundum $GaFeO_3$ displaying magnetoelectric coupling"

Hongjun Niu[1], Michael J. Pitcher[1], Alex J. Corkett[1], Sanliang Ling[2], Pranab Mandal[1], Marco Zanella[1], Karl Dawson[3], Plamen Stamenov[4], Dmitry Batuk[5], Artem M. Abakumov[5,6], Craig L. Bull[7], Ronald I. Smith[7], Claire A. Murray[8], Sarah J. Day[8], Ben Slater[2], Furio Cora[2], John B. Claridge[1,*] and Matthew J. Rosseinsky[1,*]

[1]Department of Chemistry, University of Liverpool, Crown Street, Liverpool L69 7ZD, UK

[2]Department of Chemistry, University College London, Gower Street, London WC1E 6BT, UK

[3]Centre for Materials and Structures, School of Engineering, University of Liverpool, Liverpool L69 3GH, UK

[4]CRANN, Trinity College Dublin, College Green, Dublin 2, Republic of Ireland

[5]EMAT, University of Antwerp, Groenenborgerlaan 171, 2020 Antwerp, Belgium

[6]Skoltech Center for Electrochemical Energy Storage, Skolkovo Institute of Science and Technology, 143026 Moscow, Russian Federation

[7]ISIS Neutron and Muon Source, Science and Technology Facilities Council, Rutherford Appleton Laboratory, Harwell Oxford, Didcot, Oxfordshire OX11 0QX, UK

[8]Diamond Light Source, Diamond House, Harwell Oxford, Didcot, Oxfordshire OX11 0DE, UK

Contents

Additional computational details and results

Energetics of cation swaps (defect formation)

Both ambient phase and corundum-type structure of $GaFeO_3$ contain octahedral Ga and Fe sites, a feature that could allow significant disorder in the cation distribution. Corundum, $LiNbO_3$ and ilmenite structures share the same oxygen sublattice, but correspond to different arrangements of the Ga and Fe ions. $LiNbO_3$ and ilmenite are long-range ordered phases, while corundum corresponds to complete disorder of the cation distribution. Phases with partial $LiNbO_3$-type order are identified as polar corundum. In our computational work, site occupancy is defined relative to the fraction of Fe ions in each cation configuration that corresponds to Fe sites in the polar $LiNbO_3$ phase (*i.e*. a value of 1 corresponds to a fully ordered $LiNbO_3$ configuration). In addition to cation order, the magnetic moment of the Fe^{3+} ions can give rise to ferro-, antiferro- and para-magnetic phases that have been investigated by selecting the relevant spin orientation of the Fe ions in the unit cell.

The first part of our computational study considered the long-range ordered $LiNbO_3$ and ilmenite phases of $GaFeO_3$ and $ScFeO_3$. The magnetic ground state for both compositions is found to be FM in the ilmenite and AFM in the $LiNbO_3$ cation arrangement, with the latter being the ordered phase with lowest energy for both $GaFeO_3$ and $ScFeO_3$.

The calculated bond lengths in the AFM $LiNbO_3$ structure are reported in Table S1. Fe-O bond lengths are more commensurate with Ga-O than Sc-O distances: the Fe-O1 bond length in $ScFeO_3$ is shorter than Sc-O1 by over 0.1 Å, while in $GaFeO_3$ the differences between Fe-O and Ga-O bond lengths are within 0.02 Å. The different ionic sizes are reflected in the stable crystal structures of the binary oxides: both α-Fe_2O_3 and α-Ga_2O_3 adopt the corundum structure, while corundum-type Sc_2O_3 is not known.

The energetics of cation disorder in $GaFeO_3$ and $ScFeO_3$ is summarised in Table S2. The case of $ScFeO_3$ has already been examined[1], where we have shown that the ground state for cation order is the $LiNbO_3$ structure, and cation disorder is dominated by "anti-site" occupation of Sc/Fe ions within a pair (dimer) of face-shared octahedra. This type of defect is indicated as C in Table S2 and has a formation energy of 544 meV in $ScFeO_3$. The corresponding C defect in $GaFeO_3$ has a much lower calculated formation energy of 205 meV. The energy cost of an anti-site defect in the $AlFeO_3$-type structure of $GaFeO_3$ is even smaller at 185 meV (see Table S2), which may be responsible for the partial site occupancies observed experimentally in the ambient phase of $GaFeO_3$.[2]

Cation order is coupled with magnetic order. The $LiNbO_3$ phase has AFM coupling of the Fe^{3+} spins, while ilmenite has FM coupling. The anti-site C defect creates an ilmenite nucleus in the $LiNbO_3$ phase, and is stabilised by spin inversion at the Fe^{3+} cation (this combination is indicated as C+S in Table S2), yielding a formation energy of -26 meV in $GaFeO_3$. A spin AFM Fe^{3+} pair (D in Table S2) is also calculated to be more stable than the AFM $LiNbO_3$ order 29 meV. In fully ordered $ScFeO_3$, the same C+S and D defects are energetically unfavourable by 339 and 365meV, respectively, because of the larger energy cost of the Sc-Fe site swap.

In addition to isolated defects, we considered the energetics of defect clusters, comprising more than one antisite defect in adjacent sites. The combination of configurational and magnetic terms in a 2 × 2 × 1 supercell with 24 formula units makes it impossible to study every combination of cation and spin distribution; we have therefore applied a knowledge-led search to identify stable defect configurations, where we started from a single C+S defect configuration (see Table S2), and we gradually created one, two and three additional C+S defects in the cell at different positions. Knowledge of the most stable configuration in the cell with N defects was used to guide the search for the most stable configurations in a cell with N+1 defects. We found that from one to four C+S defects per cell, it is progressively more favourable to create additional antisite defects in the same (001) atomic layer. In other words, the presence of one C+S defect is able to seed a cluster of units with FM ilmenite order within the AFM $LiNbO_3$ matrix. The spin inversion in neighbouring antisite defects is stabilised by the overall stability of FM order in the (001) plane and AFM between adjacent (001) atomic layers. This interaction favours the propagation of antisite defect clusters in the (001) plane. The most stable defect configuration for the cell with four C+S defects (see Figure S1b) features full (001) layers of Ga/Fe cations (in the 2 × 2 × 1 supercell each (001) atomic layer contains 4 metal cations). The creation of this defect is energetically favourable by 162.4 meV, or 40.6 meV per antisite defect, compared to 26 meV for the isolated antisite defect. These energy values are relatively small, hence we may expect the propagation of antisite defects along (001) planes to be disrupted by thermal disorder and entropic terms, leading to partial short but not long-range cation order in the structure.

Configurational sampling of cation order

To complete the study of relative stability for different cation distributions in $GaFeO_3$ and $ScFeO_3$, we performed a full search of the configurational space of these compositions in the

corundum structure. All possible cation permutations were considered within a single hexagonal unit cell (6 formula units), and for each cation permutation all possible paramagnetic spin solutions (with equal number of spin-up and spin-down Fe^{3+} cations) were considered. This produced 2331 configurations with distinct cation and spin orders for each material, which were generated using the SimDope code[3]. The polar $LiNbO_3$ and non-polar ilmenite structures are two of the 2331 configurations generated this way. We computationally screened the relative stabilities of all these configurations, using a coarser computational setting (cFIT3 auxiliary basis set, 2 Å cutoff radius, 1.0×10^{-5} Ha SCF convergence and 2.0×10^{-3} Ha $Bohr^{-1}$ for geometry optimisations). These less computationally intensive calculations give very well correlated results on relative energies and geometries in comparison with the most computationally expensive and accurate production quality settings (Figure S2).

In Figure 3 we show the relative stabilities of different cation configurations of $ScFeO_3$ and $GaFeO_3$ as a function of normalised site occupancies, defined as the proportion of Fe^{3+} cations in a given configuration that are coincident with Fe^{3+} positions in the fully ordered $LiNbO_3$ structure. For $ScFeO_3$, this systematic examination indicates that the $LiNbO_3$ structure is the most stable configuration, consistent with experimental evidence. In $GaFeO_3$ the most stable configuration corresponds to phase separation of the Ga and Fe ions into distinct Fe_2O_3 and Ga_2O_3 [001] layers (see Figure S3), as a consequence of the small energy cost of Ga/Fe site swaps being counterbalanced by strong magnetic coupling between adjacent Fe^{3+} ions. Calculations using a larger ($2 \times 2 \times 2$) supercell, predict that further separation into 12 atomic layers thick Fe_2O_3 and Ga_2O_3 slabs is energetically more stable by 18 meV/f.u. relative to the 6 atomic layers thick solution allowed by the $2 \times 2 \times 1$ supercell, due to enhanced magnetic coupling of Fe^{3+} cations.

Configurational entropies

Analysis of the above results relative to cation (dis)order suggest that the cation arrangement in corundum-type $GaFeO_3$ can be represented by a model of perfect solid solution of Ga_2O_3 and Fe_2O_3, due to the commensurate ionic radii of Ga^{3+} and Fe^{3+}. However, in $LiNbO_3$-type $ScFeO_3$, the entropy stabilisation should be estimated based on a solid solution $A_xB_{1-x}O_3$ of heteronuclear Fe-Sc dimers, where A and B correspond to the two possible orientations of each dimer[1]. This leads to an entropy stabilisation of $2kT \times \ln 2$ (143 meV/f.u. at a synthesis temperature of 1200 K) for $GaFeO_3$, and of $kT \times \ln 2$ (106 meV/f.u. at a synthesis temperature of 1773 K) for $ScFeO_3$. In the ambient pressure $AlFeO_3$-type $GaFeO_3$, cation permutations (*i.e.*

formation of anti-site defects) are limited to octahedral Fe and Ga sites that correspond to all Fe and half the Ga ions, with the other half being tetrahedral. Therefore, the configurational entropy of the ambient pressure $AlFeO_3$-type $GaFeO_3$ can be estimated as $-3/2 \times kT \times [1/3 \times \ln(1/3) + 2/3 \times \ln(2/3)]$ (98.8 meV/f.u. at a synthesis temperature of 1200 K).

Supporting Figures

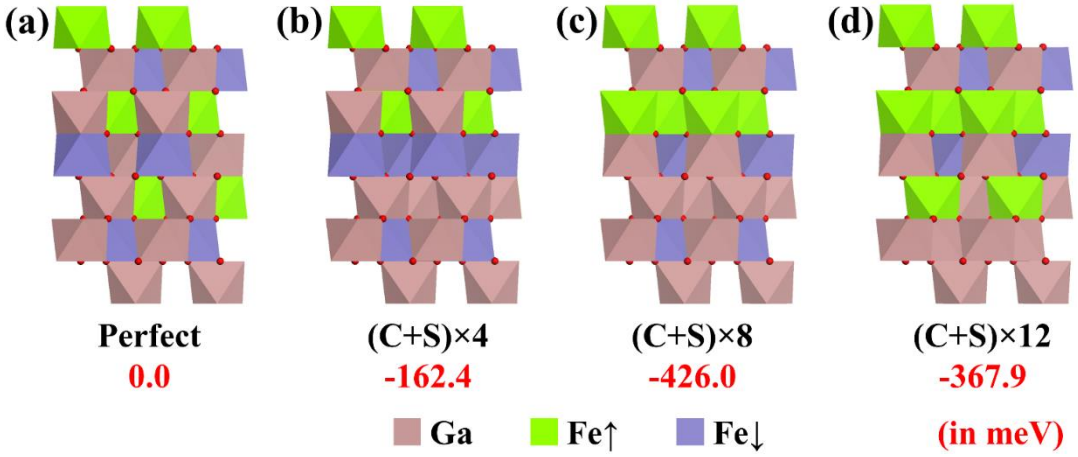

Figure S1: Polyhedral representation of the perfect and defective $GaFeO_3$ corundum lattices with different numbers of anti-site defects accompanied with spin inversions on Fe^{3+} cations. The numbers in red indicate the defect formation energies (in meV) with respect to the perfect lattice.

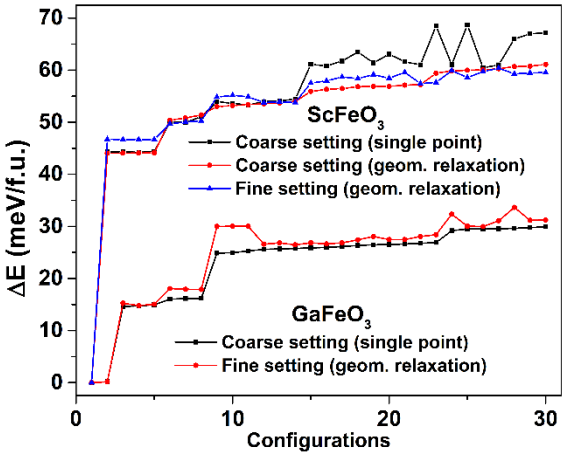

Figure S2: Relative energy of the 30 most stable cation configurations in $GaFeO_3$ and $ScFeO_3$ (among the 2331 sampled), calculated with different computational settings.

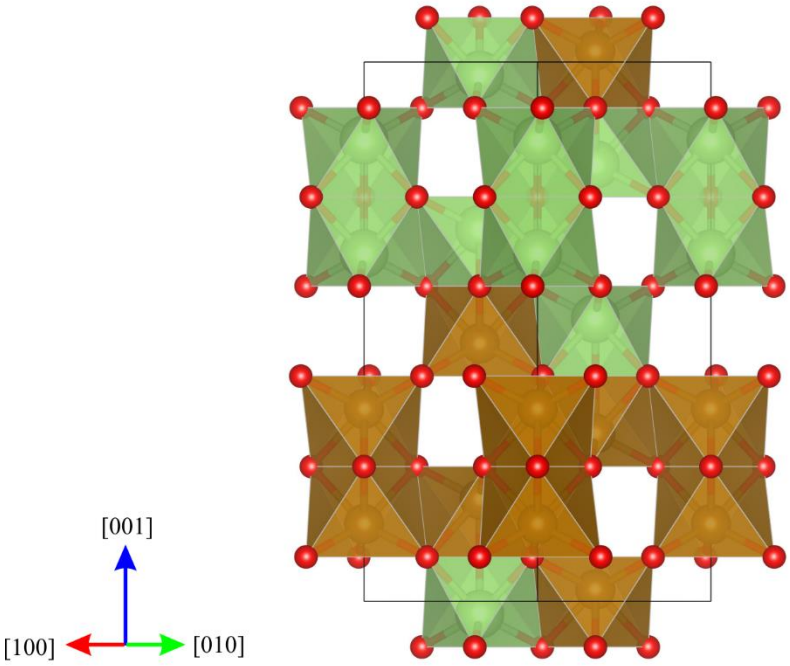

Figure S3: The calculated ground state configuration of $GaFeO_3$ in a hexagonal corundum-type cell, which is phase separated into distinct α-Fe_2O_3 (brown) and α-Ga_2O_3 (green) blocks. This does not occur in $ScFeO_3$, as the energy barrier to Sc/Fe swaps is much higher than for Ga/Fe swaps, and the corundum-type Sc_2O_3 structure is much less stable than α-Ga_2O_3.

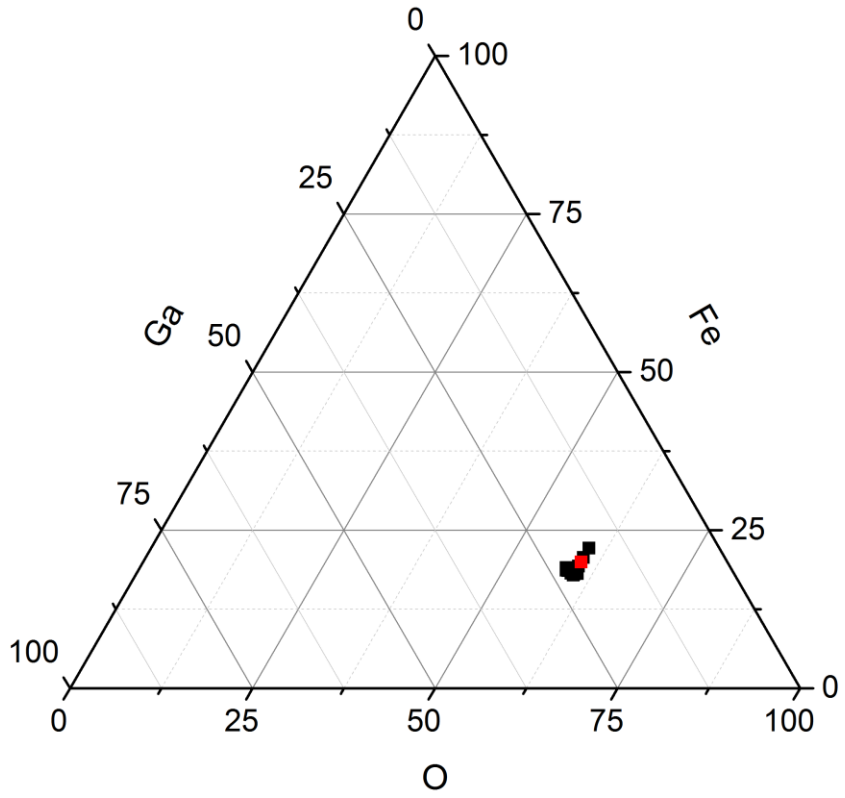

Figure S4: The composition of $GaFeO_3$ with polar corundum structure, from TEM-EDX analysis of 25 particles. Black markers correspond to observed points. The red marker is the mean composition obtained from the 25 points, $Ga_{1.08(5)}Fe_{0.94(5)}O_{2.99(2)}$.

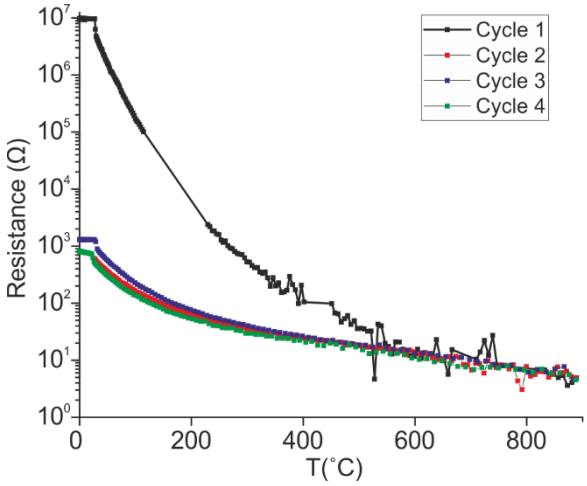

Figure S5: Resistance of a sample of $GaFeO_3$ measured in-situ at 6 GPa, over four consecutive heating cycles. The resistance of the first heating cycle coincides with that of the subsequent cycles at ~550 °C, consistent with the formation of the corundum phase at this temperature.

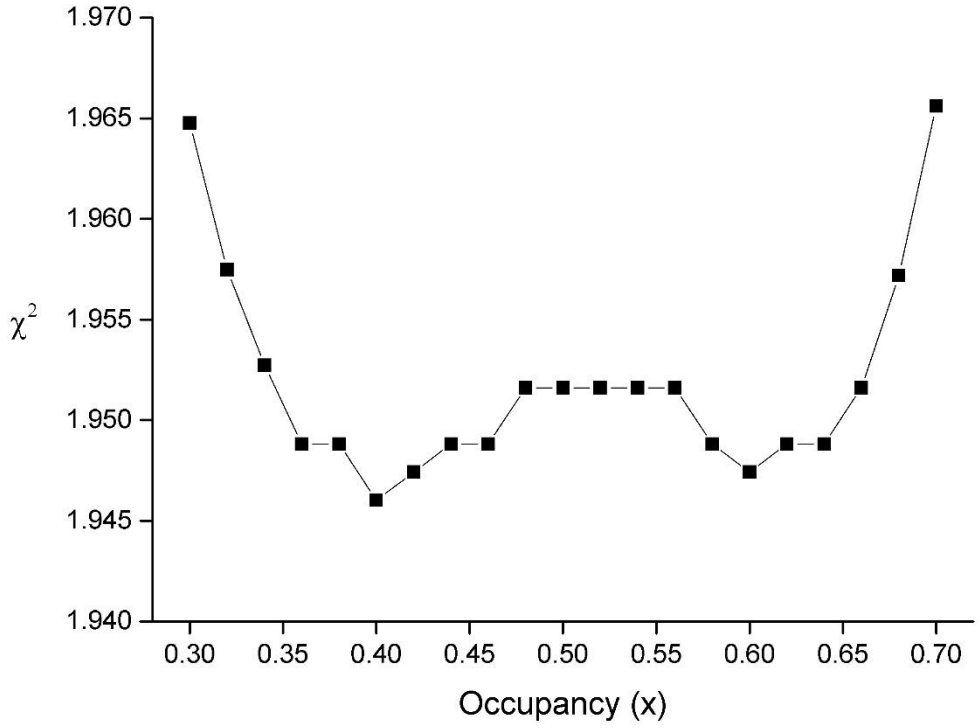

Figure S6:Agreement factors (χ^2) obtained by imposing fixed cation occupancies on the *R*3*c* model $[Ga_{1-x}Fe_x][Ga_xFe_{1-x}]O_3$, from Rietveld refimenent against SXRD anomalous scattering data.

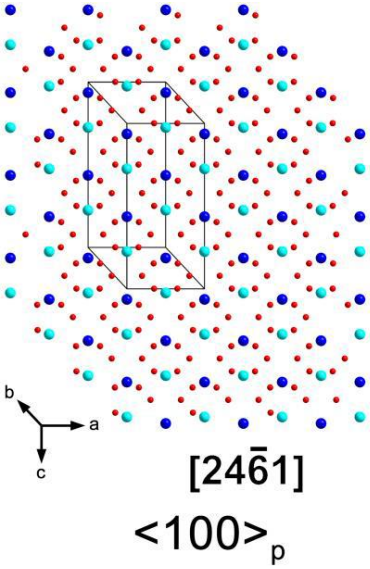

Figure S7: Structure projections where the two different Fe/Ga positions form separate atomic columns.

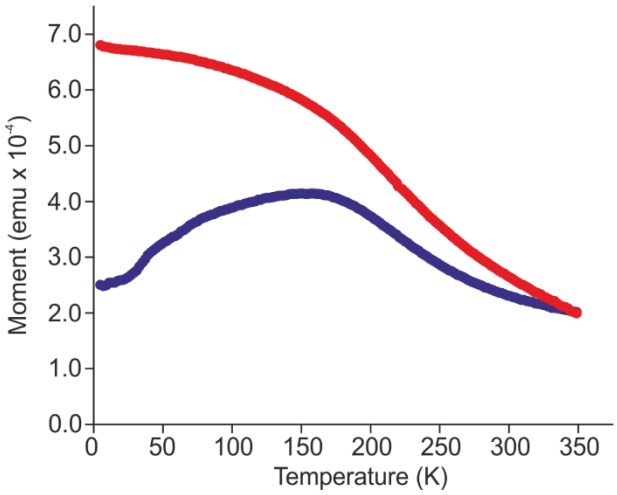

Figure S8: Magnetization of $GaFeO_3$ in the range 5 – 350 K, under an applied magnetic field of 100 Oe. ZFC (blue) and FC (red) data are plotted.

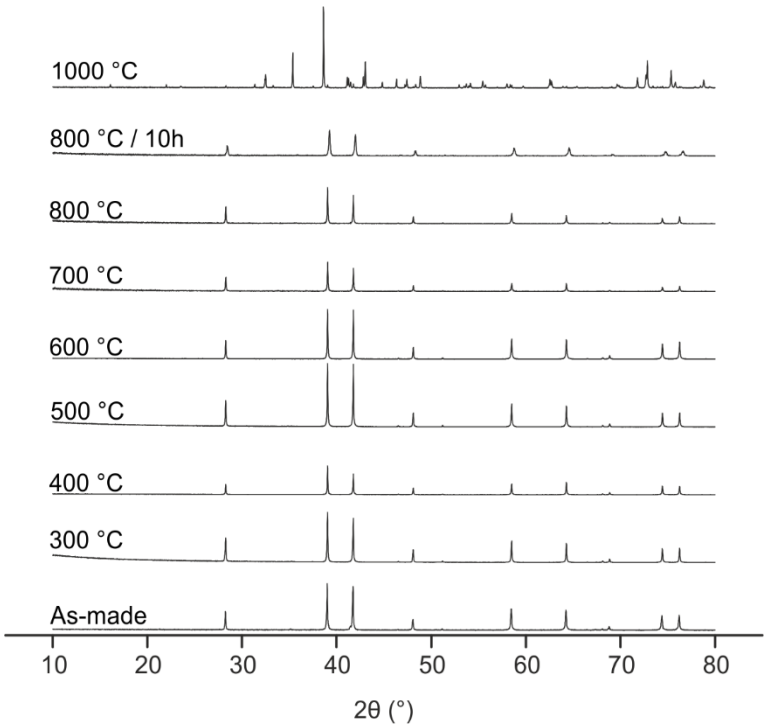

Figure S9: Laboratory PXRD patterns of polar corundum $GaFeO_3$ annealed at different temperatures for 1 hour, and an additional long (10 h) annealing at 800 °C. The corundum structure is retained up to 800 °C, but the ambient pressure $AlFeO_3$ phase is recovered after annealing at 1000 °C.

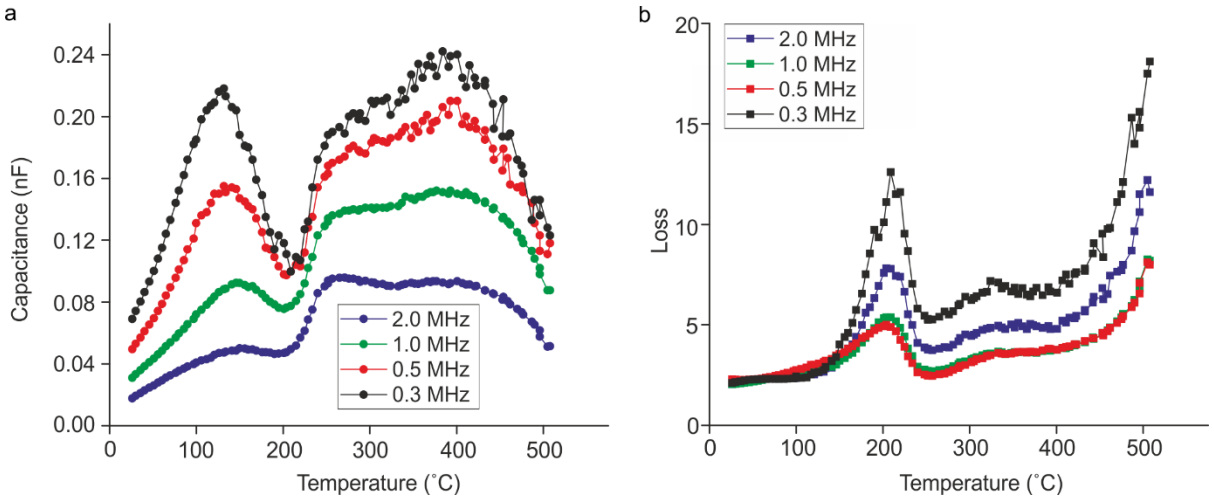

Figure S10: Frequency dependence of (a) capacitance and (b) loss for a pellet of polar corundum $GaFeO_3$ measured on heating from 25 °C. The peak at ~200 °C occurs at all frequencies.

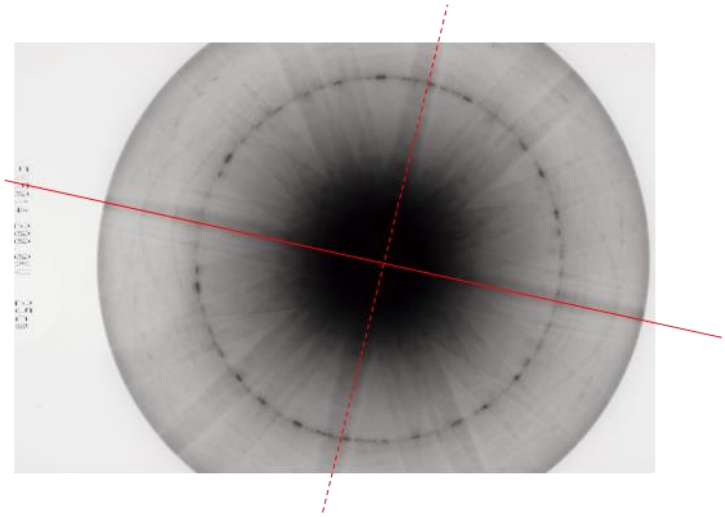

Figure S11: CBED whole pattern symmetry from the [$\bar{1}$11] zone of an annealed polar corundum $GaFeO_3$ sample. This exhibits only 1 mirror plane (solid red line), consistent with 3*m* point symmetry. The dashed line is the missing orthogonal mirror plane whose presence would confirm $\bar{3}m$ point symmetry.

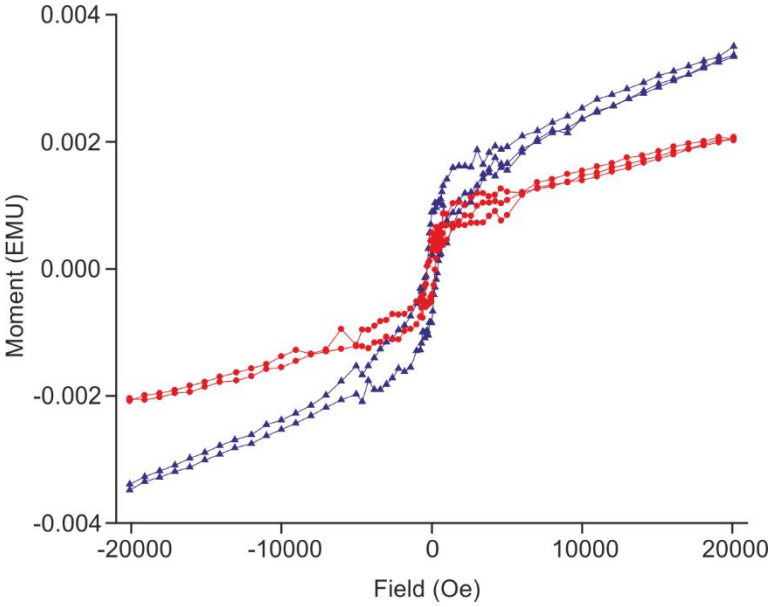

Figure S12: Magnetisation versus temperature for a sample of corundum GFO after heating in the DSC instrument to 800 K, showing retention of weak ferromagnetism. Blue points = 10 K, red points = 200 K.

Supporting Tables

Table S1: Selection of DFT optimised bond lengths in $LiNbO_3$–ordered $ScFeO_3$ and $GaFeO_3$.

$ScFeO_3$	**Bond Lengths (Å)**	**$GaFeO_3$**	**Bond Lengths (Å)**
Fe-O1	1.95	Fe-O1	1.95
Fe-O2	2.12	Fe-O2	2.10
Sc-O1	2.07	Ga-O1	1.93
Sc-O2	2.16	Ga-O2	2.09

Table S2: Selected defect formation energies in polar corundum $ScFeO_3$ and $GaFeO_3$ and in ambient pressure $AlFeO_3$-type $GaFeO_3$ determined at the PBE0 level of theory. S indicates the spin inversion of one Fe^{3+} cation; C the creation of one antisite defect; C+S the creation of an antisite defect accompanied by spin inversion at the Fe^{3+} cation; DIMER the creation of a spin antiferromagnetic homonuclear ($2\times Fe^{3+}$) pair; DIMER+S the creation of a spin ferromagnetic (FM) homonuclear ($2\times Fe^{3+}$) pair. For the ambient pressure $AlFeO_3$-type $GaFeO_3$, antisite defects are only considered for Ga/Fe on the octahedral sites, and the two sets of values provided represent two symmetry inequivalent octahedral sites of Fe^{3+}. A positive value indicates the defect formation is endothermic, and a negative value indicates the defect formation is exothermic.

$ScFeO_3$ ($LiNbO_3$-type)	**$E_{def} - E_{ideal}$ (meV)**	**$GaFeO_3$ ($LiNbO_3$-type)**	**$E_{def} - E_{ideal}$ (meV)**	**$GaFeO_3$ ($AlFeO_3$-type)**	**$E_{def} - E_{ideal}$ (meV)**
S	286	S	243	S	277 / 218
C	544	C	205	C	185 / 302
C+S	339	C+S	-26	C+S	292 / 187
DIMER	365	DIMER	-29		
DIMER+S	640	DIMER+S	211		

Table S3 Compositional analysis of $GaFeO_3$ by ICP-OES measurements. Numbers in brackets represent one standard deviation. The "standard" sample is a stoichiometric mixture of Ga_2O_3 and Fe_2O_3.

Sample	**Ga / ppm**	**Fe / ppm**	**Formula**
Blank	0.32(1)	0.70(1)	-
Standard	16.9(1)	13.60(2)	$Ga_{0.997(8)}Fe_{1.002(8)}O_3$
$GaFeO_3$ starting batch	17.4(1)	13.6(1)	$Ga_{1.012(12)}Fe_{0.988(12)}O_3$
ANV478	41.5(2)	34.1(5)	$Ga_{0.994(18)}Fe_{1.006(18)}O_3$
ANV498	39.1(4)	31.5(1)	$Ga_{1.004(13)}Fe_{0.996(13)}O_3$

Table S4: Agreement factors for corundum $GaFeO_3$ (sample 1) refined against room temperature NPD data in disordered ($R\bar{3}c$), $LiNbO_3$ ordered (polar corundum, $R3c$) and $FeTiO_3$ ordered (ilmenite, $R\bar{3}$) models.

	$R\bar{3}c$	$R3c$	$R\bar{3}$
R_{wp}	5.136	5.044	5.119
χ^2	3.206	3.095	3.187

Table S5: Agreement factors for corundum $GaFeO_3$ (sample 2) refined against room temperature NPD data in disordered ($R\bar{3}c$), $LiNbO_3$ ordered (polar corundum, $R3c$) and $FeTiO_3$ ordered (ilmenite, $R\bar{3}$) models.

	$R\bar{3}c$	$R3c$	$R\bar{3}$
R_{wp}	6.294	6.244	6.273
χ^2	1.127	1.109	1.119

References

1. Li, M.-R.; Adem, U.; McMitchell, S. R. C.; Xu, Z.; Thomas, C. I.; Warren, J. E.; Giap, D. V.; Niu, H.; Wan, X.; Palgrave, R. G.; Schiffmann, F.; Cora, F.; Slater, B.; Burnett, T. L.; Cain, M. G.; Abakumov, A. M.; van Tendeloo, G.; Thomas, M. F.; Rosseinsky, M. J.; Claridge, J. B., *Journal of the American Chemical Society* **2012,** *134* (8), 3737-3747.

2. Mohamed, M. B.; Senyshyn, A.; Ehrenberg, H.; Fuess, H., *Journal of Alloys and Compounds* **2010,** *492* (1–2), L20-L27.

3. Enciso-Maldonado, L.; Dyer, M. S.; Jones, M. D.; Li, M.; Payne, J. L.; Pitcher, M. J.; Omir, M. K.; Claridge, J. B.; Blanc, F.; Rosseinsky, M. J., *Chemistry of Materials* **2015,** *27* (6), 2074-2091.